Chapter 12
Heterostructures

The interface is the device.

H. Kroemer [961]

Abstract Heterostructures are the most important basis for modern devices and are covered regarding various aspects including heteroepitaxy on planar and patterned substrates, surfactants, heterostructure band lineup as well as energy levels and recombination in planar confined systems (quantum wells and two-dimensional electron gases).

12.1 Introduction

Heterostructures consist of (at least two) different materials. The geometry of the interfaces between the two materials can be complicated. The simplest case is a planar interface, i.e. a layered system. A metal–semiconductor junction is generally a heterostructure. However, we will use the term mostly for structures of various semiconductors. Most of the heterostructures discussed here are epitaxial, i.e. fabricated by the successive epitaxy of the various layers on a substrate. Another method to fabricate heterostructures of different (and dissimilar) materials is wafer bonding that is briefly discussed in Sect. 12.6.

Many modern semiconductor devices rely on heterostructures, such as the heterobipolar transistor (HBT), the high electron mobility transistor (HEMT), lasers and nowadays also light-emitting diodes. Shockley had already considered heterostructures in his 1951 patent for pn-junctions. For the development and the realization of heterostructures H. Kroemer and Zh.I. Alferov were awarded the 2000 Physics Nobel Prize. The properties of charge carriers in layers that are part of heterostructures can be quite different from those in bulk material, e.g. extremely high mobility, high radiative recombination efficiency or novel states of matter, as revealed in the quantum Hall effects.

M. Grundmann, *The Physics of Semiconductors*, Graduate Texts in Physics,
DOI 10.1007/978-3-319-23880-7_12

12.2 Heteroepitaxy

12.2.1 Growth Methods

Since the thickness of layers in the active part of heterostructures has to be controlled to monolayer precision and the thickness of layers can go down to the single monolayer range, special growth methods have been developed [962–964]. Among these molecular beam epitaxy (MBE [965]), chemical vapor deposition (CVD [966, 967]) and metalorganic vapor phase epitaxy (MOVPE [968]) are the most common for Si, Ge, III–V and II–VI semiconductors. In particular, oxide semiconductors are also fabricated with pulsed laser deposition (PLD [969]). Liquid phase epitaxy (LPE [970]) used to be very important for the fabrication of LEDs but has lost its role largely to MOVPE.

MBE is performed in an ultrahigh vacuum (UHV) chamber, pumped by getter pumps and cryo-shrouds. The source materials are evaporated from effusion cells and directed towards the heated substrate. If the source materials are supplied as a gas stream, the method is called gas-source MBE (GSMBE). If metalorganic compounds are used as precursors, the method is denoted as MOMBE. The atoms impinge on the substrate with thermal energy and are first physisorbed. After diffusion on the surface they either desorb or they are chemisorbed, i.e. incorporated into the crystal. In order to obtain high spatial homogeneity of material properties such as composition, thickness and doping, the substrate is rotated during deposition.

During CVD and MOVPE the heated substrate is in a gaseous environment. The transport gas is typically H_2, N_2 or O_2. Precursor materials are hydrides such as silane, germane, arsine or phosphine (SiH_4, GeH_4, AsH_3, PH_3) and (for MOVPE) metalorganic compounds, such as, e.g. trimethylgallium (TMG). Due to the toxicity of the hydrides, alternative, i.e. less-toxic and less-volatile compounds are used, such as TBAs ($(CH_3)_3CAsH_2$). The crystal growth occurs after pyrolysis and catalysis of the compounds close to or on the substrate surface. All remaining C and H atoms (and whatever else that is not incorporated into the crystal) leave the reactor and are neutralized and stopped in a scrubber.

In-situ monitoring is of importance to obtain information about the growth process while it is underway. Using the information in a feedback loop it is possible to achieve in-situ control of the process, e.g. for precise determination of growth rates or layer thickness. Techniques are RHEED (reflection high-energy electron diffraction) [971] (only for UHV systems) and RAS (reflection anisotropy spectroscopy) [972, 973].

12.2.2 Substrates

Thin-film epitaxy is mostly performed on wafers, i.e. thin circular slices of substrate material. The most common substrate materials are Si (currently up to 400 mm diameter [974, 975]), Ge (also up to 300 mm [976]), GaAs (up to 6 inch), InP (up to 4 inch)

and sapphire (up to 6 inch). Typical wafer thickness is 300–500 μm. Also, very thin, flexible Si wafers (8–10 μm) have been developed [977]. A wafer is cut from a large single cylindrical crystal that is fabricated with suitable growth techniques such as Czochralski (CZ) growth (1918) modified by Teal and Little [978, 979]. In CZ growth the crystal is pulled from a seed crystal out of a melt of previously polycrystalline, pure or doped material. All dislocations stop in the narrow neck between the seed and the main body of the cylinder. The diameter of the crystal is controlled by the pulling rate and the heating power. For the growth of III–V compound semiconductors liquid encapsulated CZ (LEC) growth has been developed to counteract the high volatility of the growth-V component. During LEC growth the melt is completely covered with molten boric oxide (B_2O_3). The keys to optimization of the crystal growth process are numerical modeling and computer control. In Fig. 12.1a,c a large CZ silicon crystal and a smaller LEC GaAs crystal (boule) are shown. Over time wafer size and ingot mass have increased remarkably (Fig. 12.1b). For details on other important fabrication methods for bulk crystals, including float-zone (FZ [980]) or vertical gradient freeze (VGF), we refer to the literature [981]. Significant expertise is necessary for cutting, grinding and polishing (lapping) wafers for epitaxy.

For semiconductors, the wafer is marked with *flats* to indicate orientation and doping. In Fig. 12.2 the standard flats are shown for (100)- and (111)-oriented material. The primary (major) flat (OF, orientation flat) defines the crystallographic

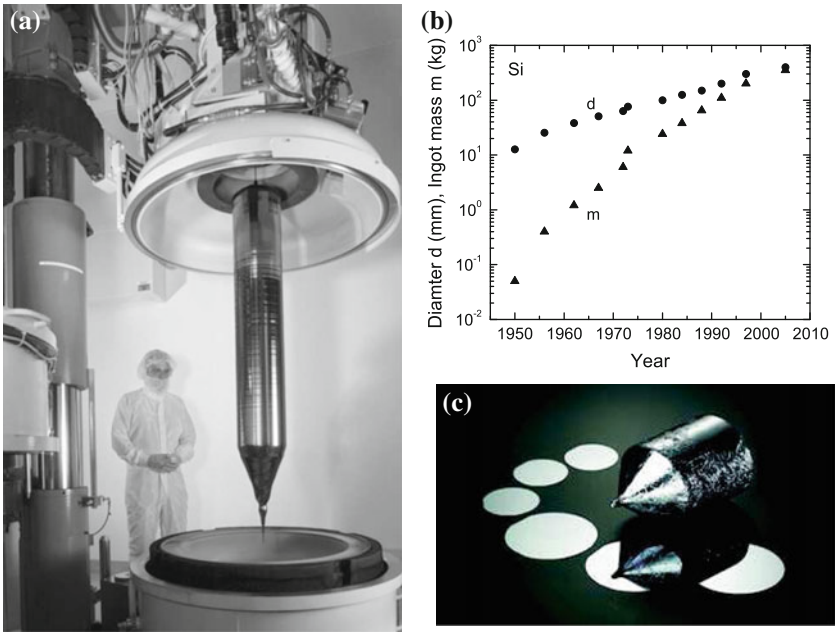

Fig. 12.1 (**a**) Silicon single crystal for 300-mm diameter wafers after opening of the crucible. From [982] with permission. (**b**) Historic development (first year of larger production) of silicon wafer diameter and ingot mass. Data from [975]. (**c**) GaAs single crystal (boule) for 4-inch wafers and some cut and polished wafers

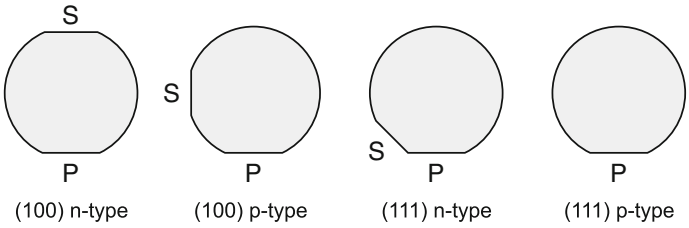

Fig. 12.2 Schematic semiconductor wafer geometry for various orientations and doping with the primary (P) and secondary (S) flats indicated

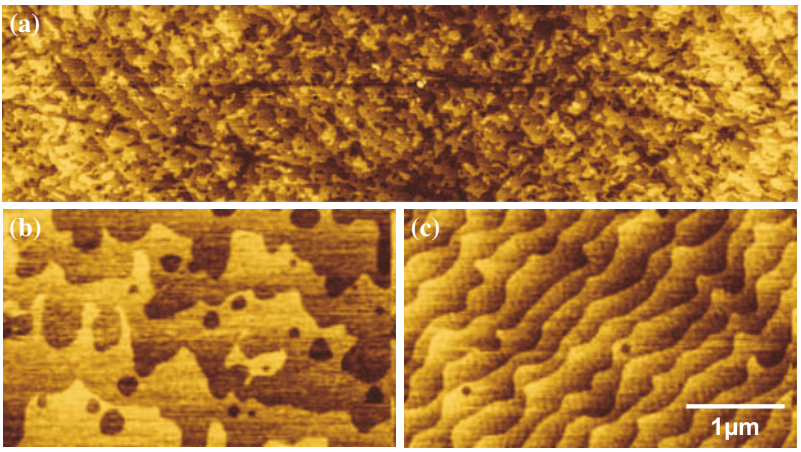

Fig. 12.3 (**a**) AFM images of an as-received ZnO wafer, exhibiting small terraces and nm deep scratches from polishing. (**b**, **c**) Two ZnO $(000\bar{1})$ wafers with vicinal surfaces after thermal treatment (1000 °C for 2 h in O_2), exhibiting atomically flat terraces with $c/2$ monoatomic step heights. Two different substrates with different off-cut (misorientation direction and angle) are shown. Adapted from [990]

orientation[1] is longer than the secondary (minor) flat which defines the conductivity type (IF, identification flat). For a 4-inch (100 mm) diameter wafer the OF is 32 and the IF 12 mm long. The front surface, on which the epitaxy is performed, typically undergoes an elaborate cleaning and polishing process. Silicon processes [981, 984] are based on the RCA cleaning procedure [985] and the related Shiraki etch [986] and can achieve clean, atomically flat surfaces [987]. III-V semiconductors are typically prepared using a polishing etch [988, 989], often solutions containing bromine. It is possible to create compound semiconductor surfaces that exhibit large, essentially monoatomically flat terraces between individual surface steps. Polishing or other surface damage can also be removed prior to epitaxy with thermal (Fig. 12.3) or ion beam treatments.

[1] In the 'US' flat definition, the primary flat is the $(01\bar{1})$ surface, in the 'EJ' definition, the primary flat is $(0\bar{1}\bar{1})$.

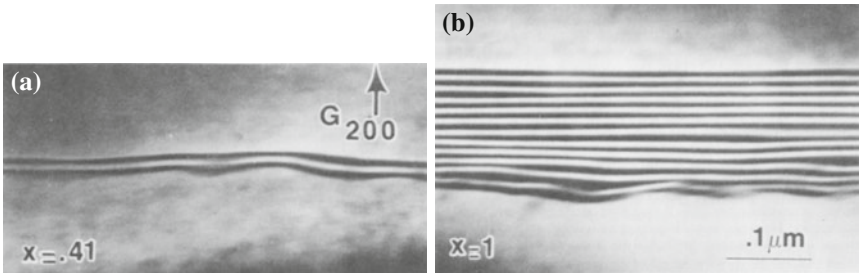

Fig. 12.4 Cross-sectional TEM of MBE-grown $Al_xGa_{1-x}As$/GaAs heterostructures for (**a**) $x = 0.41$ and (**b**) $x = 1.0$. Using an AlAs/GaAs superlattice an excellent flattening of substrate roughness is achieved. From [991]

One prerequisite for making high-quality heterostructures with thin layers is a flat surface. Even if the polished substrate is not perfect, flat interfaces can be achieved with the growth of appropriate superlattice buffer layers (Fig. 12.4). Roughness can exist on all length scales and is typically investigated using atomic force microscopy scans.

High throughput demands and the advent of multi-wafer reactors make prior cleaning and etching procedures tedious. For this purpose, substrates for well-developed material systems are offered 'epiready'. Epiready wafers are often covered with a very thin protective film that can be released using a thermal treatment at or below typical growth temperature in the growth reactor immediately prior to epitaxy. The protective film separates the polished semiconductor wafer from the ambient. Examples are a few monolayers of arsenic on GaAs or two monolayers GaN on SiC. However, the suitability of a purchased substrate may depend on the duration and conditions of its storage.

A special case is the use of *curved* substrates which allow the study of growth on different crystal orientations in a continuous fashion. Such experiments have been performed using cylindrical substrates [992] and hemispherical crystals. For the latter homoepitaxy has been reported for Si [993, 994], SiC [995] or GaAs [996]. Also heteroepitaxy has been investigated, for example for GaP and GaAs on Ge [997] (cmp. Fig. 12.12). Using such curved substrates, the growth rate can be determined as a function of crystal orientation as shown for GaAs (on GaAs) in Fig. 12.5; large differences are found for (111)A and (111)B surfaces. For growth of silicon the variations with angle are much smaller in the range of 10 % [992].

12.2.3 Growth Modes

The growth of a material A on a material B can occur via three fundamental growth modes (Fig. 12.6), the layer-by-layer or Frank-van der Merwe (FvdM) growth mode [384], the island or Volmer-Weber (VW) growth mode [998] and the

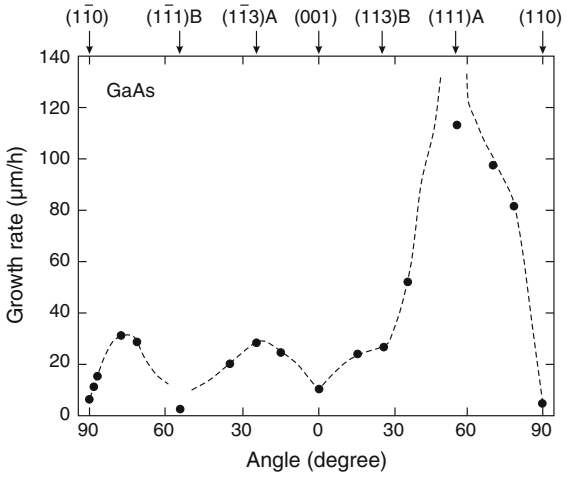

Fig. 12.5 Growth rate of GaAs in vapor phase transport at 725° as a function of crystal orientation. The *dashed line* is guide to the eyes. Adapted from [996]

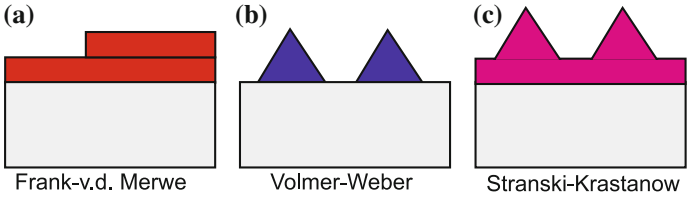

Fig. 12.6 Schematic of the three different fundamental epitaxial growth modes

Stranski-Krastanow (SK) growth mode [999]. In [999] the possibility of island formation on an initially flat heteroepitaxial surface was proposed for the growth of lattice-*matched* ionic crystals that have different charges. The term SK growth is now typically used in lattice-*mismatched* heteroepitaxy for the island formation (and related relaxation of strain energy, cmp. Fig. 14.26) on an initially two-dimensional layer (wetting layer).[2] Also growth of islands *relaxed* by misfit dislocations in strained heteroepitaxy has been termed SK growth [1000].

The growth mode is determined by the relation of the free energies (per area) of the surface σ_s, interface σ_i and film σ_f. Wetting of the substrate and growth of a coherent film (FvdM-growth) occurs for

$$\sigma_s > \sigma_i + \sigma_f. \tag{12.1}$$

If the inequality has the opposite sign, Volmer-Weber or Stranski-Krastanow growth occurs. Additionally the strain energy of the film must be considered. The SK growth

[2]This is the growth mode of self-assembled epitaxial quantum dots as discussed in Sect. 14.3.3.

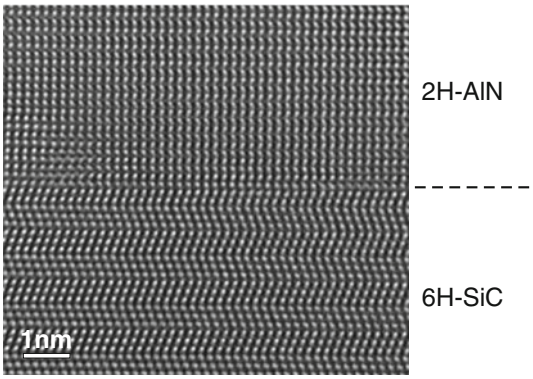

Fig. 12.7 HRTEM cross section of the interface region of MOVPE grown hexagonal AlN on 6H-SiC substrate. Adapted from [1004]

generally occurs when there is wetting of the substrate but layer strain is unfavorable and leads to islanding.

Layer-by-layer growth typically involves nucleation of two-dimensional islands and 'filling' of the remaining monolayer before the next one is started. Another growth mode resulting in smooth epitaxial layers is step-flow growth where adatoms are incorporated mainly at step edges. A more detailed discussion can be found in [1001]. Further details on crystal growth can be found in [1002].

The nucleation and the initial film growth are important and determine the film quality. Several techniques have been developed to overcome common problems. A typical strategy is the growth of a low-temperature nucleation layer.

12.2.4 Heterosubstrates

If homosubstrates are not available or very expensive, semiconductors are grown on dissimilar substrates, e.g. (Al,Ga)N and ZnO on sapphire (Al_2O_3) or SiC.[3] In Fig. 12.7 the interface region of hexagonal AlN on 6H-SiC (cmp. Fig. 3.28b) is shown. The change of crystallographic phase is obvious; the perfect atomic arrangement justifies the term 'epitaxy', literally meaning 'order on top'.

In many cases, the integration of III–V- or II–VI-based semiconductors for optoelectronic applications on silicon for electronic devices is desirable, such as GaAs/Si, InP/Si, GaN/Si or the growth on economic substrates is attractive such as GaN/Al_2O_3 and ZnO/Al_2O_3. For all such combinations the epitaxial relationship, i.e. the alignment of the crystallographic directions of both materials, which can have different space groups, has to be considered. Some examples for epitaxial relationships are given in Table 12.1. The epitaxial relation is determined by the energetically favorite formation of the interface and the early stages of growth.

[3] For ZnO, homosubstrates have recently been produced with 3-inch diameter [1003].

Table 12.1 Epitaxial relationship for various film/substrate combinations, ZnO (or GaN) on *c*-, *a*- and *r*-sapphire and Si(111)

ZnO	Al_2O_3 [00.1]	ZnO	Al_2O_3 [11.0]	ZnO	Al_2O_3 [10$\bar{1}$.2]	ZnO/GaN	Si [111]
[00.1]	[00.1]	[00.1]	[11.0]	[11.0]	[10$\bar{1}$.2]	[00.1]	[111]
[11.0]	[01.0]	[11.0]	[00.1]	[00.1]	[01$\bar{1}$.1]	–/ [21$\bar{1}$.0]	[1$\bar{1}$0]

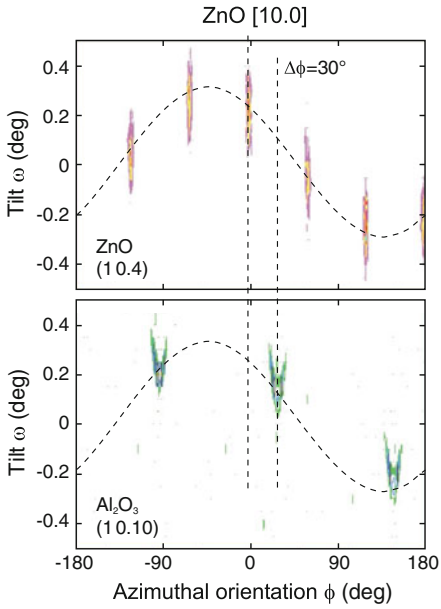

Fig. 12.8 X-ray diffraction intensity from the asymmetric ZnO (10.4) (*upper panel*) and the sapphire (10.10) (*lower panel*) reflections as a function of the azimuthal sample orientation (rotation angle ϕ around the [00.1] axis). The peaks appear at different tilt angles ω due to an overall tilt of the mounted sample (*dashed sinusoidal lines*). The ZnO [00.1] axis is not tilted with respect to the sapphire [00.1] direction

In Fig. 12.8, X-ray diffraction data are shown from a ZnO layer on *c*-oriented sapphire. The hexagonal ZnO lattice is rotated by 30° with respect to the trigonal sapphire lattice. In the case of growth of ZnO on Si(111) an amorphous SiO_2 layer can form at the interface such that the crystallographic information of the substrate is lost. The ZnO grains exhibit random in-plane orientation (Fig. 12.9).

If substrate and epilayer have different space groups, the formation of domains can occur [1006]. The two-dimensional symmetries of various substrates are listed in Table 11.1. The group theoretical minimum number of domains N_{RD} in dependence of the two-dimensional symmetries of substrate and epilayer with rotational symmetries C_n and C_m, respectively, is given by [1007]

$$N_{RD} = \frac{\mathrm{lcm}(n, m)}{m}, \tag{12.2}$$

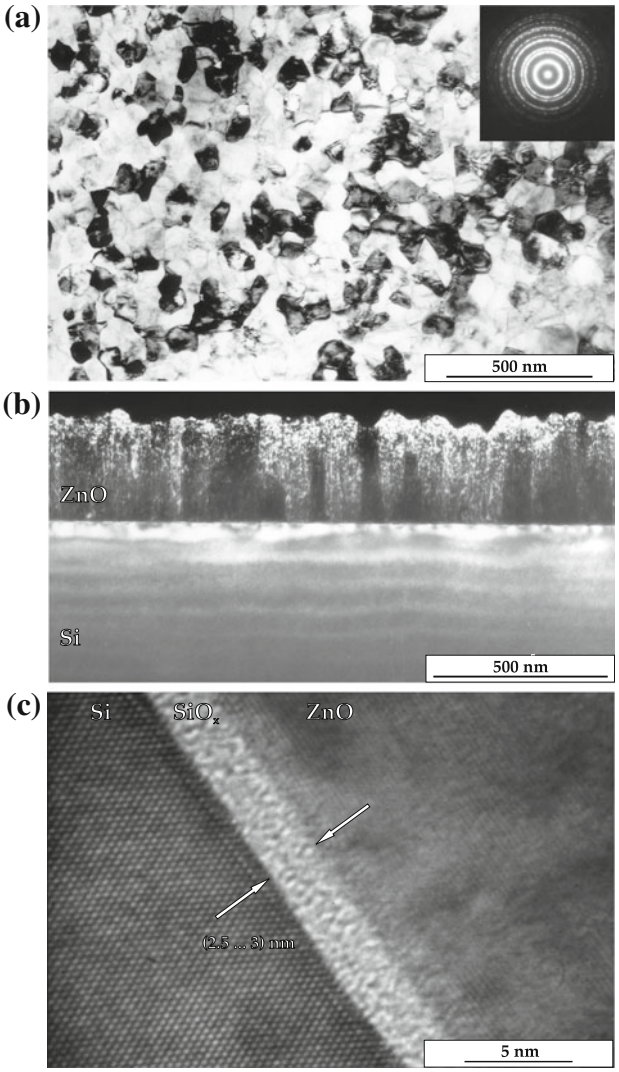

Fig. 12.9 (**a**) Plan-view TEM image (*inset*: electron diffraction diagram averaged over several grains) of ZnO on Si(111).(**b**) Cross-sectional TEM of the same sample. (**c**)High-resolution cross-sectional image of the ZnO/SiO_2/Si interface region. Adapted from [1005]

where lcm denotes the least common multiple. The values are listed in Table 12.2 and visualized in Fig. 12.10.

If the main symmetry axes of substrate and epilayer are not aligned, mirror domains appear. An example is the growth of GaN(00.1) on Ge(111), for which it has been reported that the major symmetry directions do not align exactly. There is a 4° in-plane rotation of the lattices with respect to the usual [11.0] ∥ [$1\bar{1}0$] in-plane relationship [1008] (cmp. the exact alignment for GaN/Si(111) in Table 12.1).

Table 12.2 Number of rotational (or mirror) domains N_{RD} for all 2D point groups of substrate (G_S) (rows) and epilayer (G_E) (columns). When two numbers are given ($x|y$), the first (second) number represents the number of domains if mirror symmetry planes of substrate and epilayer align (misalign).

$G_S \backslash G_E$	1	m	2	2 mm	3	3 m	4	4 mm	6	6 mm
1	1	1	1	1	1	1	1	1	1	1
m	2	1|2	2	1|2	2	1|2	2	1|2	2	1|2
2	2	2	1	1	2	2	1	1	1	1
2 mm	4	2|4	2	1|2	4	2|4	2	1|2	2	1|2
3	3	3	3	3	1	1	3	3	1	1
3 m	6	3|6	6	3|6	2	1|2	6	3|6	2	1|2
4	4	4	2	2	4	4	1	1	2	2
4 mm	8	4|8	4	2|4	8	4|8	2	1|2	4	2|4
6	6	6	3	3	2	2	3	3	1	1
6 mm	12	6|12	6	3|6	4	2|4	6	3|6	2	1|2

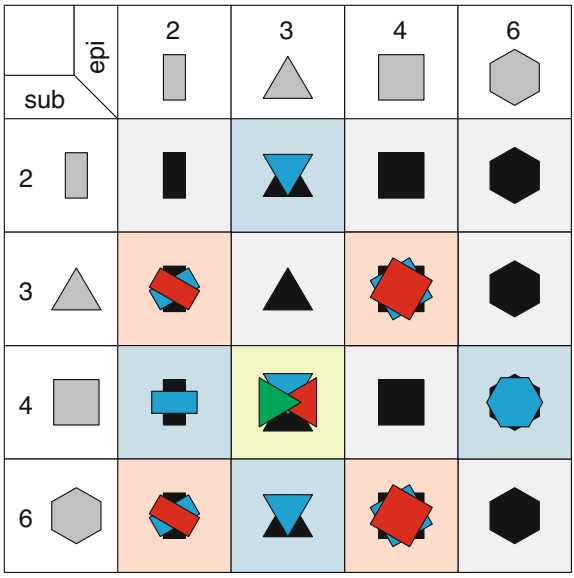

Fig. 12.10 Visualization of the minimum number of rotational domains for different substrate and epilayer symmetries according to Table 12.2

Due to 3 m mirror symmetry of the substrate, the misaligment is equivalent for clockwise and counter-clockwise rotation. Therefore two domains with an angle of 8° occur (Fig. 12.11).

Another well-known domain effect in heteroepitaxy is the occurrence of antiphase domains of zincblende semiconductors (e.g. GaAs, GaP, InP,...) grown on Si(001) with monoatomic steps; such surface actually exhibits two kind of terraces (1×2 and 2×1 reconstructions) and is thus itself not homogeneous. The formation of antiphase domains can be avoided by using an off-cut of the surface against the (001)-planes promoting double-atomic steps [1009]. In Fig. 12.12a the growth of GaP on a Ge

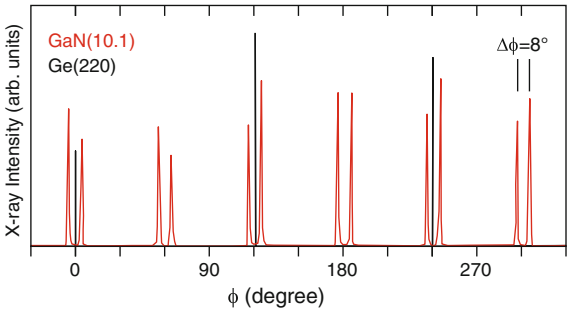

Fig. 12.11 X-ray diffraction ϕ-scans of GaN(00.1)/Ge(111). Adapted from [1008]

hemisphere with [111]-pole is depicted; spherical triangles meeting at the ⟨100⟩ poles can be seen. In a similar experiment GaAs was grown in a spherical depression in Ge(001) (Fig. 12.12b), allowing a more detailed look at the [001]-pole. Close to the it, within an approximately square area, antiphase domains (cmp. Sect. 4.4.4) form. Along the connection lines between different ⟨001⟩-poles, an antiphase domain boundary forms, microscopically broken up into domains [997].

Details of the initial deposition steps can determine the orientation in polar materials. GaN directly grown on c-Al_2O_3 grows with N-face orientation (see Fig. 3.19). The high surface mobility of Ga allows nitrogen to take its preferred position in the first atomic layer. Even under Ga-rich conditions the N atoms can kick-off the Ga from its favorite site on the surface. If an AlN buffer is used the strong bond between Al and oxygen leads to an Al atomic layer at the interface and subsequent GaN grows with a Ga-face [1010].

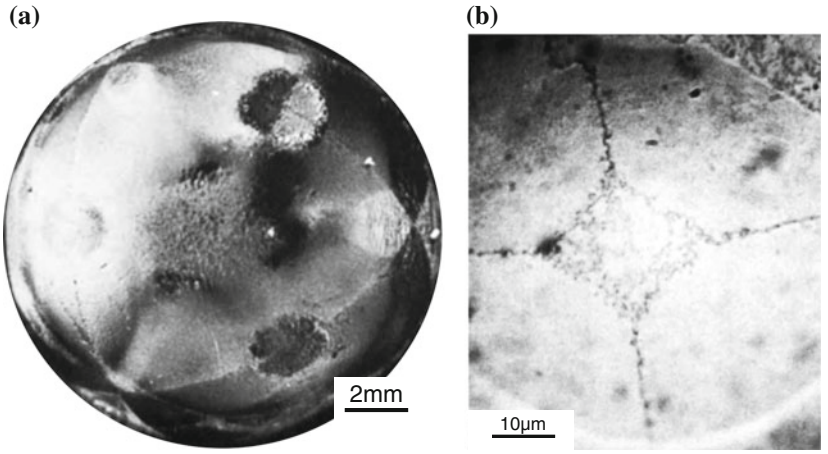

Fig. 12.12 The morphology of (**a**) GaP grown on a Ge hemisphere with [111]-pole and (**b**) GaAs grown in a Ge(001) spherical depression. Adapted from [997]

12.2.5 Patterned Substrates

Using patterning of the substrate certain growth modes and crystallographic directions of the growth front can be evoked.

Returning to the discussion of [00.1] or [00.$\bar{1}$] growth of wurtzites, on a sapphire substrate with lateral AlN patterns, laterally orientation-modulated GaN can be grown (Fig. 12.13). At the juncture of the phases an inversion domain boundary forms [1011].

The defect density can be reduced in parts of the structure using epitaxial lateral overgrowth (ELO) [1013]. The defects thread only from the limited contact area of the layer with the substrate and the part of the layer away from the mask ('wing') is free of defects (Fig. 12.14).

While the patterning of a mask may be cumbersome and require interruption of growth, the in-situ deposition of a random SiN mask with small holes has been found beneficial in the epitaxy of GaN [1014]. GaN islands nucleate selectively in the mask openings (Fig. 12.15a). The nucleation and subsequent coalescence of islands (Fig. 12.15b) leads to defect annihilation and eventually again to a flat film (Fig. 12.15c). The reduction of defect density is evident (Fig. 12.15d) and leads to improved optical properties [1015].

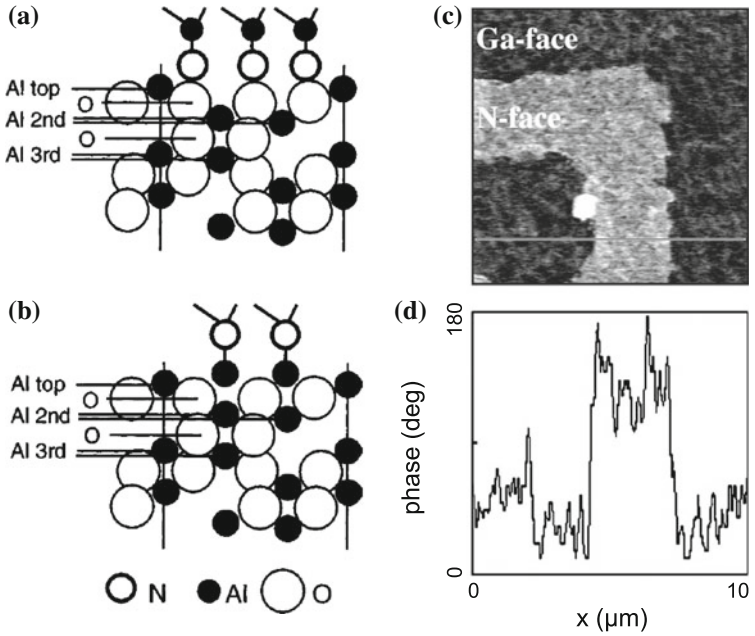

Fig. 12.13 Side view of the heterointerfaces between AlN and *c*-oriented sapphire with nitrogen (**a**) and Al (**b**) being the first layer. Adapted from [1010]. (**c**) Phase image of piezoresponse force microscopy (PFM) of lateral polarity GaN heterostructure and (**d**) linescan of phase signal along *white line* in part (**c**). Adapted from [1012], part (**c**) reprinted with permission, © 2002 AIP

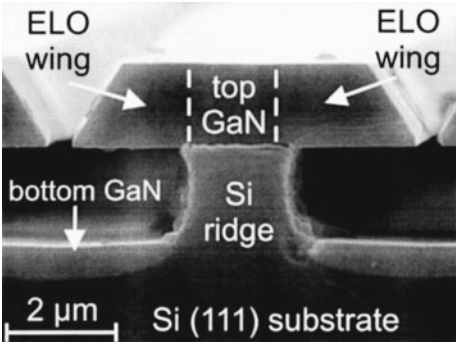

Fig. 12.14 SEM cross-sectional image of GaN grown on a structured Si(111) substrate. The laterally grown wings extend about 2.5 µm over the grooves. The thickness of the GaN layer is 0.5 µm on the bottom of the grooves, while it is 1.4 µm on top of the ridges. Reprinted with permission from [1013], © 2001 AIP

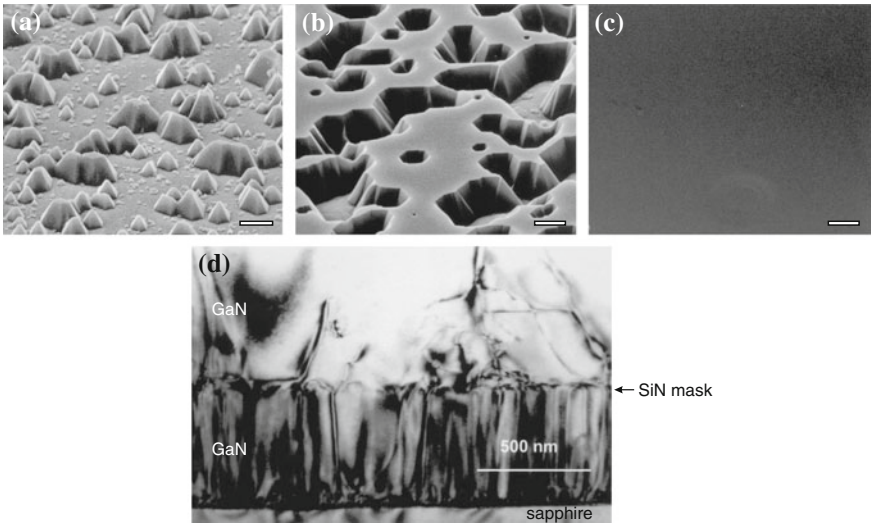

Fig. 12.15 SEM images of GaN (**a**) growing through the openings of a random SiN mask, (**b**) laterally overgrowing the mask and coalescing and (**c**) eventually forming a flat film. Bar widths are 2, 1 and 10 µm. (**d**) Cross-section TEM image. Adapted from [1014]

Using patterned substrates with stripe-like mesas and promoting the growth on a sidewall of the mesa, the direction of GaN growth front can be steered into a semipolar direction (cmp. Sect. 15.4.3). The r-plane sapphire substrate with etched mesa stripes oriented along the [11.0] direction exposes [00.1]-oriented sidewall facets on which the GaN grows along its *c*-axis; The angle of 57.6° between the r- and the c-planes of sapphire is very close to the angle (3.21c) of 58.4° between the GaN semipolar (11.2) and the (00.1) plane. The flat growth front represents a

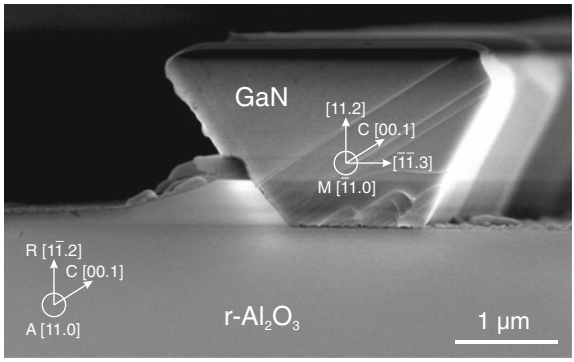

Fig. 12.16 SEM cross-sectional image of MOVPE GaN grown on patterned r-sapphire exposing a (11.2) growth front. Based on SEM image courtesy of F. Tendille

(11.2) facet [1016] (Fig. 12.16). After coalescence of grains from various mesas, a flat (11.2) surface arises, allowing the reduction of various defects including basal stacking faults [1017, 1018].

12.2.6 Pseudomorphic Structures

Heterostructures can generally be made from any sequence of materials. However a mismatch in lattice constant (or a different crystal structure) leads to strains and stresses that are of the order of 10^3 atmos for strains of 1 % ($\sigma \sim C\epsilon$, $C \approx 5 \times 10^{10}$ Pa) as discussed in Sect. 5.3.3. The total strain energy is $\propto C\epsilon^2$. Above a critical thickness $h_c \propto \epsilon^{-1}$ (cf. Sect. 5.4.1) defects, e.g. misfit dislocations (relaxing strain with their edge components), are generated (Sect. 12.2.7). There are a number of semiconductor combinations that are lattice matched and thus can be grown with arbitrary thickness. $Al_xGa_{1-x}As$ is closely lattice matched to GaAs for all Al concentrations. See Fig. 6.21 for lattice-matched pairs, e.g. $In_{0.53}Ga_{0.47}As$/InP. Often, thin layers of lattice-mismatched materials with thickness smaller than the critical thickness are used.

For many device applications the ability to grow pseudomorphic layers thicker than the critical layer thickness would be beneficial. The use of compliant substrates was proposed in [1019] to meet this demand. A recent review on compliant substrate technologies can be found in [393]. Schemes to accommodate part of the mismatch strain in the substrate include the use of cantilevered membranes, silicon-on-insulator, twist bonding, glass bonding or trenched substrates. In this sense also nanowhiskers (Sect. 14.2.3) represent a compliant substrate, enabling the growth of coherent (laterally confined) layers thicker than the critical thickness of a 2D layer (cmp. Fig. 14.9).

12.2.7 Plastic Relaxation

Above the critical thickness, a film will relax plastically by forming misfit dislocations. The cross-hatch pattern at the surface due to misfit dislocations is shown in Fig. 12.17. A TEM image of an array of misfit dislocations can be found in Fig. 5.33b.

The strain relaxation in mismatched heteroepitaxy can be determined experimentally via the wafer curvature of the heterostructure (Sect. 5.3.5). Data for the thickness dependent relaxation $\epsilon(d)$ of $In_{0.15}Ga_{0.85}As$ on GaAs (mismatch $\approx 1\%$) are shown in Fig. 12.18. Growth interruptions lead to larger relaxation at smaller thickness. Therefore relaxation at early times or small thickness (above h_c) is kinetically hindered, i.e., the available dislocation density and glide velocity are not sufficient to relieve the strain. At large thickness the strain does not go to zero (saturation regime) and the film remains in a metastable, incompletely relaxed state as discussed in more detail in [1020].

An extreme case of plastic relaxation is cracking (Sect. 4.4.1) which can occur for example in thick films during cooling due to the mismatch of the thermal expansion coefficients of substrate and epilayer (Fig. 12.19). Such cracking can be avoided by the introduction of suitable stress-relaxing layers and growth on predefined mesas [1021, 1022].

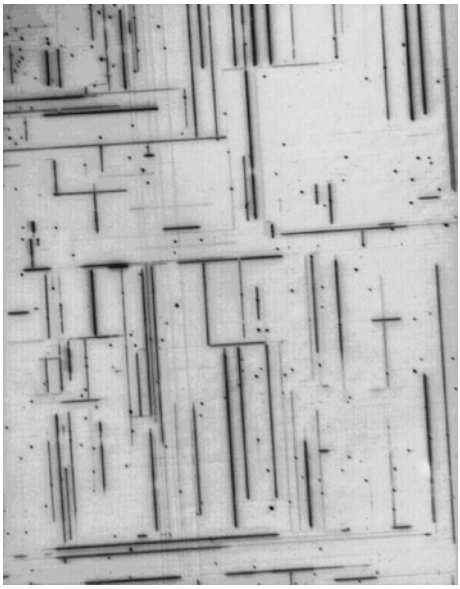

Fig. 12.17 Optical image of the surface of a supercritical, plastically relaxed $In_xGa_{1-x}As$ film on GaAs. Image width is about 1 mm. The cross-hatch pattern is due to misfit dislocations along [110] and [1$\bar{1}$0]. A pseudomorphic layer would exhibit no contrast under the given conditions

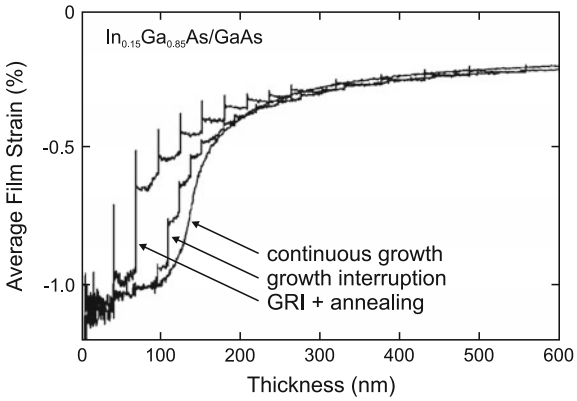

Fig. 12.18 Average film strain (measured in-situ via substrate curvature) of $In_{0.15}Ga_{0.85}As/GaAs$ grown at 450°C as a function of film thickness (determined from growth time × deposition rate). Relaxation for three different growth modes are shown (as labeled): continuous growth, employment of several growth interruptions (GRI) and GRI with annealing step (to 550°). Adapted from [1020]

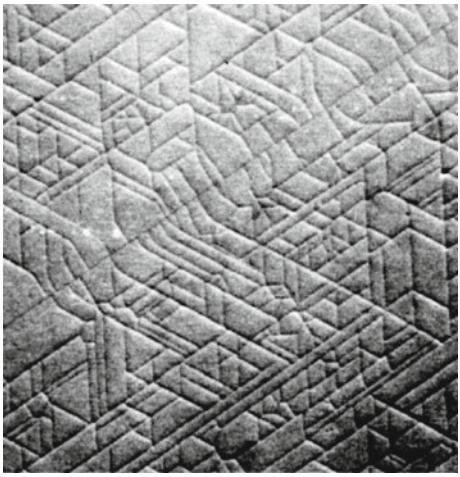

Fig. 12.19 $1 \times 1\ mm^2$ top view with a differential interference contrast microscope of a 1.3-μm thick GaN layer grown on Si(111). Reproduced with permission from [1021], © 2000 IPAP

12.2.8 Surfactants

The condition (12.1) allows layer-by-layer growth (cf. Sect. 12.2.3), i.e. the substrate surface free energy is higher than the than the total of interface and film surface free energy. This makes wetting energetically favorable. For two elements A and B, one of them must have the lower surface free energy. If A can be grown on B in Frank-van der Merwe (or Stranski-Krastanow) growth mode, then (12.1) does not hold for B on A and the growth will occur in Volmer-Weber mode, i.e. with islands. This is a serious problem for the growth of embedded layers of the type A–B–A. If the embedded film grows well, the capping does not and vice versa.

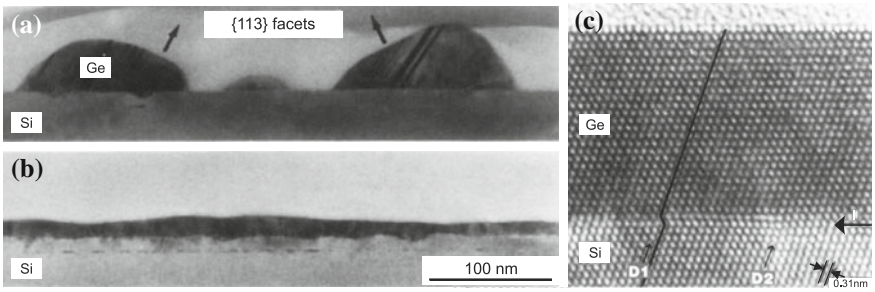

Fig. 12.20 (**a**, **b**) 10 nm thick Ge layer on Si (100) deposited at room temperature with MBE and annealed up to 770°C without (**a**) and with (**b**) Sb surfactant. Adapted from [1030]. (**c**) Cross-section TEM image of a heterostructure of 70 monolayers germanium on Si (111), grown by MBE with Sb surfactant. The *horizontal arrow* labeled 'I' denotes the position of the interface. The *arrows* labeled 'D1' and 'D2' denote the positions of partial dislocations (cmp. Fig. 4.19). Adapted from [289]

In the case of Ge on Si, Ge has the lower surface free energy than Si. Ge grows on Si in Stranski-Krastanow mode [1023] (Fig. 12.20a). Si grows both on Ge(001) and Ge/Si(001) in a Volmer-Weber mode [1024] causing severe problems for the fabrication of Si/Ge/Si quantum wells or superlattices. A substantial modification of growth mode can be achieved by using a third element C as a capping layer, saturating surface bonds. It lowers the surface free energy of both materials A and B, thus favoring wetting of the substrate. Such element C is called *surfactant* (surface-active species) [1025, 1026]. Typical examples are As [1025] or Sb [289] on Si and Ge (Fig. 12.20b). Also the surfactant modifies defect nucleation and can lead to defect-free epitaxial Ge/Si layers (Fig. 12.20c). Surfactants have also been described for the growth of compound semiconductors, e.g. In [1027] or Sb [1028, 1029] for GaAs.

12.3 Energy Levels in Heterostructures

12.3.1 Band Lineup in Heterostructures

In heterostructures, semiconductors with different band gaps are combined. The relative position of conduction and valence band (band alignment) is determined by the electron affinities χ as shown in Fig. 12.21. For a semiconductor, the electron affinity is the (positive) energy difference between vacuum level and conduction band edge. It can lead to different types of heterostructures. Early perspectives of semiconductor heterostructures are discussed in [1031].

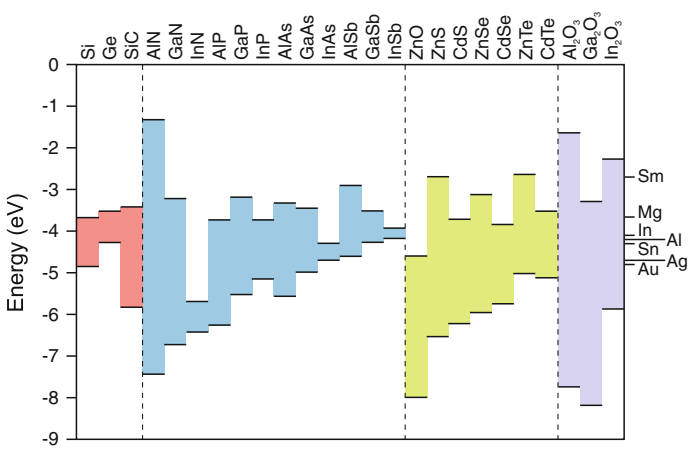

Fig. 12.21 Position of conduction and valence-band edges for a variety of semiconductors (relative to a common vacuum level at $E = 0\,\text{eV}$). Based on values from [1032], for Al_2O_3 (on InP) from [1033], for Ga_2O_3 (on GaN) from [1034] for In_2O_3 (on Si) from [1035, 1036]. On the right hand side the work functions of several metals are shown for comparison.

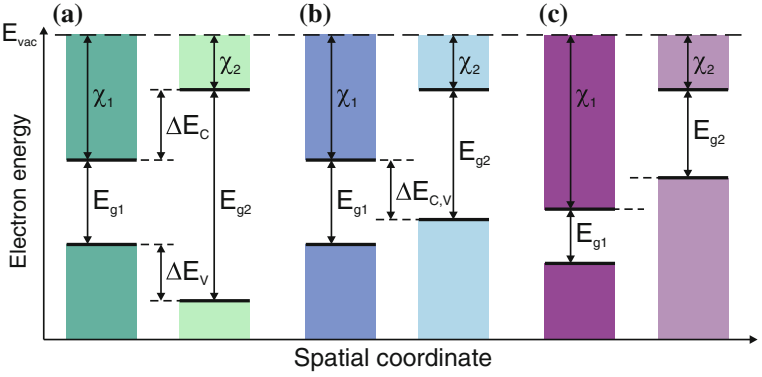

Fig. 12.22 Position of band edges (band alignment) in (**a**) type-I, (**b**) type-II and (**c**) type-III heterostructure.

In Fig. 12.22, the band alignment for type-I, type-II and type-III heterostructures are shown. In the type-I structure (straddled band lineup) the lower conduction-band edge and the higher valence-band edge are both in the material with smaller band gap. Thus, electrons and holes will localize there. In the type-II structure a staggered lineup is present and electrons and holes will localize in different materials. In the type-III structure, also termed 'broken gap' structure, the conduction band of one material is below the valence band of the other material. The technologically most relevant are type-I structures. The design of heterostructures to fulfill a certain device functionality or to have certain physical properties is called 'band gap engineering'.

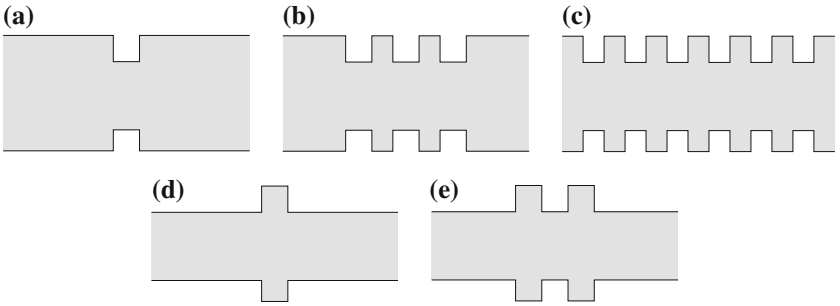

Fig. 12.23 Heterostructures with different layer sequences (band gap engineering). (**a**) quantum well (QW), (**b**) multiple quantum well (MQW), (**c**) superlattice (SL), (**d**) single-barrier tunneling structure, (**e**) double-barrier tunneling structure

In a type-I heterostructure, the conduction- and valence-band discontinuities are given, respectively, by

$$\Delta E_{\mathrm{C}} = \chi_1 - \chi_2 \tag{12.3a}$$

$$\Delta E_{\mathrm{V}} = (\chi_1 + E_{\mathrm{g}_1}) - (\chi_2 + E_{\mathrm{g}_2}). \tag{12.3b}$$

Depending on the layer sequence of high- and low-bandgap materials various configurations, as shown in Fig. 12.23 have obtained special names, such as single heterointerface, quantum well (QW), multiple quantum well (MQW), superlattice (SL). In the extreme case the layer is only one monolayer thick (Fig. 12.24) and the concept of layer and interface blurs. Such atomically precise layer sequences are mastered nowadays for a variety of material systems such as (Al,Ga)As/GaAs/InAs, InP/(In,Ga)As, Si/SiGe, ZnO/(Mg,Zn)O and also $BaTiO_3/SrTiO_3$.

The abruptness of interfaces is determined by the epitaxial machine through the switching precision of the incoming material flux and fundamentally limited by segregation phenomena which can be modeled with a segregation coefficient [1037] (cmp. Sect. 4.2.4). As shown in Fig. 12.24c, In has the tendency to be carried into the following GaAs layer. A quantitative evaluation is possible using aberration-corrected scanning transmission electron microscopy [1038].

12.3.2 Quantum Wells

The energy in a single quantum well of thickness L_z (along the growth direction z) can be calculated with the quantum-mechanical particle-in-a-box model. In the envelope function approximation (Appendix H) the wavefunction is written as a product of the Bloch function and the envelope function $\chi(z)$.

$$\Psi^{\mathrm{A,B}}(\mathbf{r}) = \exp(\mathrm{i}\,\mathbf{k}_\perp \mathbf{r})\; u_{n\mathbf{k}}(\mathbf{r})\, \chi_n(z), \tag{12.4}$$

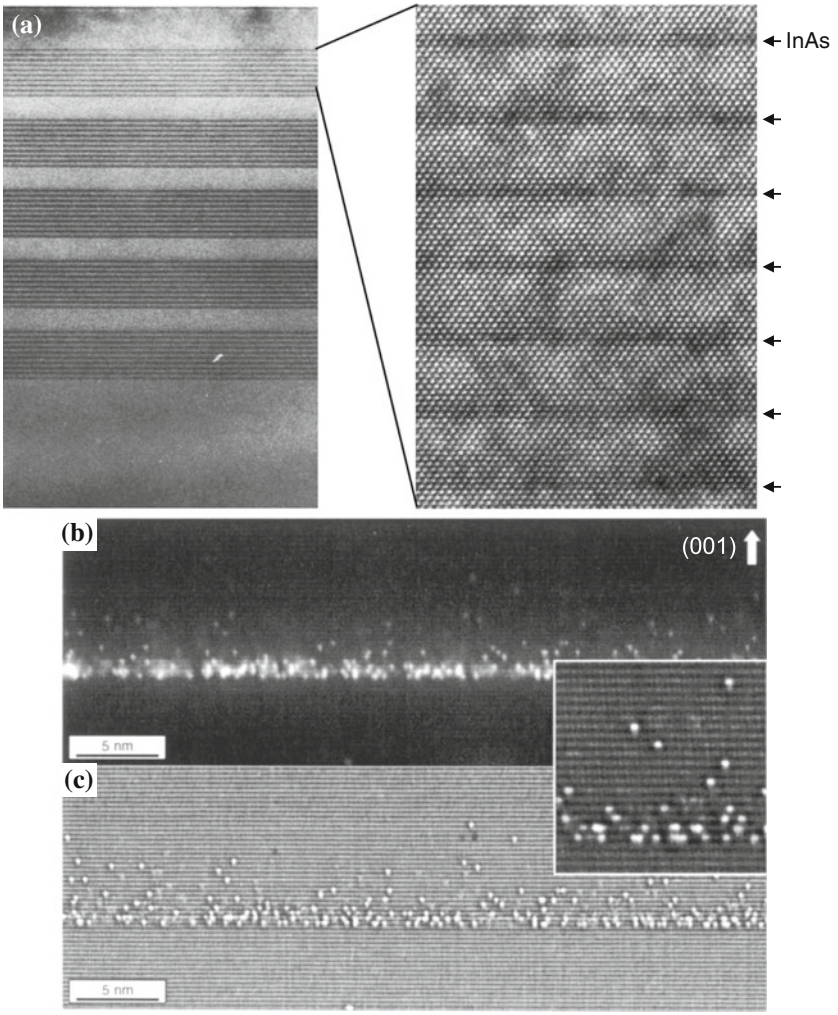

Fig. 12.24 Ultrathin heterostructures: (**a**) Cross-sectional TEM of a MOVPE-grown short-period superlattice (SPS) of InAs layers in $GaAs_{1-x}N_x$). In high resolution (*right image*), the individual rows of atoms can be seen. From [1039]. (**b**, **c**) Cross-section STM image of 2 ML InAs on GaAs; the segregation of In into the *top layer* is visible atom by atom. Adapted from [1040]

where 'A' and 'B' denote the two different materials. The envelope function χ fulfills, approximately, the one-dimensional Schrödinger-type equation,

$$\left[-\frac{\hbar^2}{2m^*}\frac{\partial^2}{\partial z^2} + V_c(z)\right]\chi_n(z) = E_n\,\chi_n(z), \tag{12.5}$$

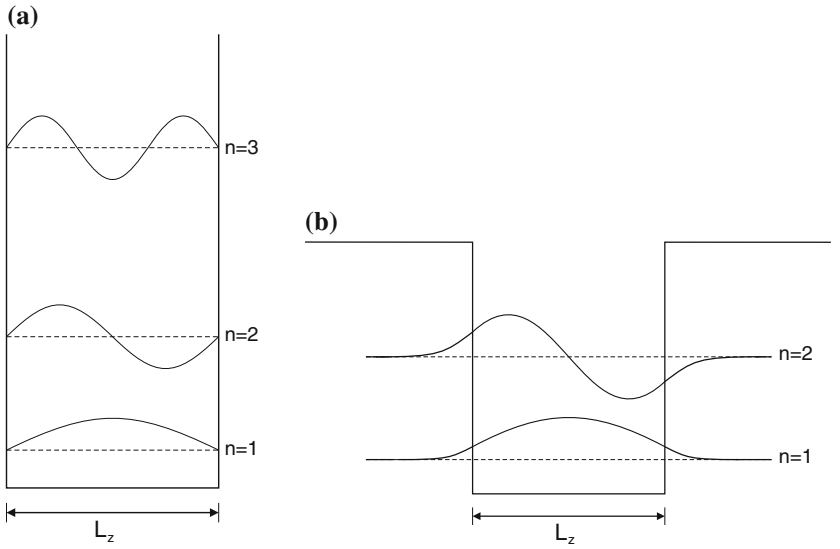

Fig. 12.25 Schematic energy levels and wavefunctions in a potential well with (**a**) infinite barriers, and (**b**) finite barrier height

where m^* denotes the effective mass. V_c is the confinement potential determined by the band discontinuities. Typically, $V_c = 0$ in the well and $V_0 > 0$ outside in the barrier. E_n are the resulting energy values of the quantized levels. In the case of infinite barriers ($V_0 \to \infty$, Fig. 12.25a) the boundary conditions $\chi(0) = \chi(L_z) = 0$ yield

$$E_n = \frac{\hbar^2}{2m^*} \left(\frac{n\,\pi}{L_z} \right)^2 \tag{12.6}$$

$$\chi_n(z) = A_n \sin\left(\frac{n\,\pi}{L_z}\, z \right), \tag{12.7}$$

where E_n is called the confinement energy.

For finite barrier height V_0 (Fig. 12.25b) the calculation leads to a transcendental equation. The wavefunction tunnels into the barrier. While for infinite barrier height the lowest level diverges for $L_z \to 0$, for finite barrier height $E_1 \to V_0$. A complication arises from the different effective mass in the well and barrier material. This is taken into account by forcing the continuity of χ and χ'/m^* across the interfaces[4] ('BenDaniel-Duke' boundary conditions [1042]). The Schrödinger equation and (semi-)analytical solutions for special and numerical methods for

[4]The kinetic energy term in (12.5) is written as $\frac{\hbar^2}{2}\,\frac{\partial}{\partial z}\,\frac{1}{m^*(z)}\,\frac{\partial \chi}{\partial z}$ for varying mass across the structure [1041].

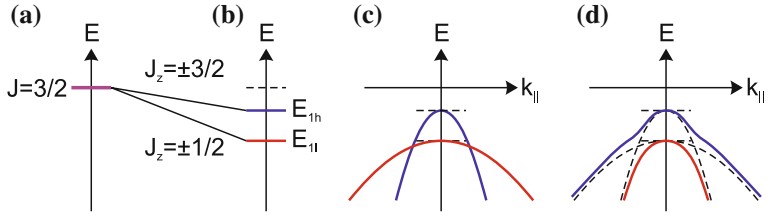

Fig. 12.26 Schematic representation of the development of hole levels in a quantum well: (**a**) degenerate bulk levels at Γ, (**b**) splitting at the subband edge (due to different quantized values of k_z), (**c**) in-plane dispersion (mass reversal), (**d**) anticrossing behavior. Based on [991]

arbitrary potential distributions are discussed in [1043]. The application of $\mathbf{k} \cdot \mathbf{p}$ theory (Appendix G) to heterostructures is discussed in [1044].

The motion of carriers in the plane is still free and has a two-dimensional dispersion. Thus, each quantized level contributes $m^*/(\pi\hbar^2)$ to the density of states at each subband edge E_n.

For holes, the situation is a little more complicated than for electrons (Fig. 12.26). First, the degeneracy of heavy and light holes is lifted since their mass enters the confinement energy. The effective hole masses along the z direction, i.e. those that enter (12.5), are

$$\frac{1}{m^z_{\mathrm{hh}}} = \gamma_1 - 2\,\gamma_2 \tag{12.8a}$$

$$\frac{1}{m^z_{\mathrm{lh}}} = \gamma_1 + 2\,\gamma_2. \tag{12.8b}$$

The light holes have the higher quantization energy. The angular momentum is quantized along the z direction. The transverse masses for the dispersion in the interface plane are

$$\frac{1}{m^{xy}_{\mathrm{hh}}} = \gamma_1 + \gamma_2 \tag{12.9a}$$

$$\frac{1}{m^{xy}_{\mathrm{lh}}} = \gamma_1 - \gamma_2. \tag{12.9b}$$

Now the heavy hole, i.e. the $J_z = \pm\frac{3}{2}$ state, has the smaller mass and the light hole ($J_z = \pm\frac{1}{2}$) the larger (Fig. 12.26c). However, this consideration is only an approximation since the lifting of degeneracy and the dispersion have to be treated on the same level. Higher terms of the perturbation calculation lead to band mixing and remove the band crossing that seems to originate from the situation at the Γ point. In reality, the bands show anticrossing behavior and are strongly deformed. The hole dispersion in a superlattice and the anticrossing behavior is shown in Fig. 12.27.

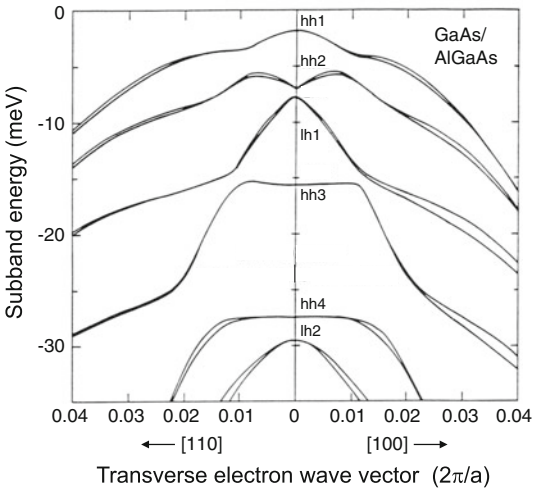

Fig. 12.27 Hole dispersion in a 68-ML GaAs/71 ML $Al_{0.25}Ga_{0.75}As$ superlattice (numerical calculation). The double curves originate from a lifting of time-reversal symmetry at $\mathbf{k} \neq 0$. Reprinted with permission from [1045], © 1985 APS

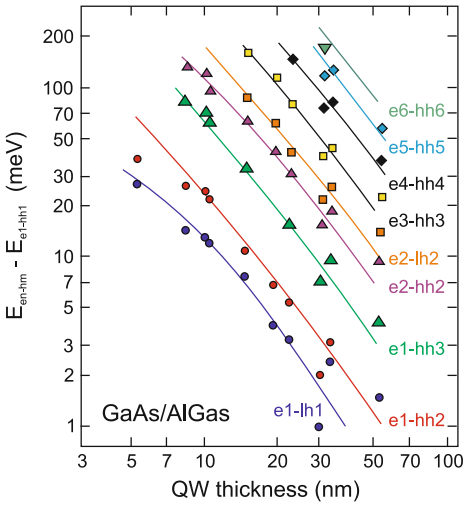

Fig. 12.28 Observed electron–hole transitions (energy difference to the first e–h transition from excitation spectroscopy) in GaAs/AlGaAs quantum wells of varying thickness. *Symbols* are experimental data, *solid lines* are theoretical model. Data from [1046]

Experimentally observed transition energies in quantum wells of varying thickness are shown in Fig. 12.28 and are in good agreement with the theoretical calculation. We note that for infinite barriers optical transitions are only allowed between confined electron and hole states with the same quantum number n. For finite barriers this selection rule becomes relaxed, and other transitions become partially allowed, e.g. e_1–hh_3. The optical matrix element from the Bloch part of the wavefunction, which was isotropic for (cubic) bulk material (9.25), is anisotropic for quantum wells. TE (TM) polarization is defined with the electromagnetic field in (perpendicular to) the plane of the quantum well (Fig. 12.29a). At the subband edge, i.e. for in-plane wavevector $k_{||} = 0$ the matrix elements for the various polarizations and propagation

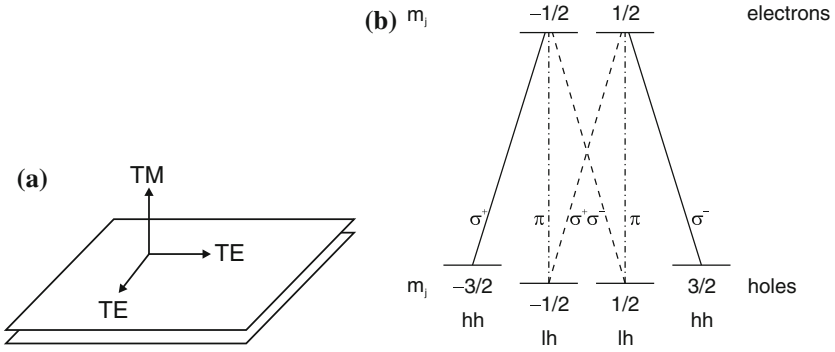

Fig. 12.29 (**a**) Directions of electric-field vector relative to the quantum-well plane for TE and TM polarization. (**b**) Optical selection rules for band–band transitions in a quantum well. If the (in-plane averaged) relative strength of the e–hh transitions (*solid lines*) is 1, the relative strength of the TE-polarized e–lh transitions (*dashed lines*) is 1/3 and that of the TM-polarized e–lh transitions (*dash-dotted lines*) is 4/3

Table 12.3 Squared momentum matrix elements $\left|\langle c|\hat{\mathbf{e}}\cdot\mathbf{p}|v\rangle\right|^2$ in a quantum well for various propagation directions in units of M_b^2. The quantum-well normal is along **z**

	Propagation	$\hat{\mathbf{e}}_x$ (TE)	$\hat{\mathbf{e}}_y$ (TE)	$\hat{\mathbf{e}}_z$ (TM)
e–hh	**x**	–	1/2	0
	y	1/2	–	0
	z	1/2	1/2	–
	x	–	1/6	2/3
e–lh	**y**	1/6	–	2/3
	z	1/6	1/6	–
	x	–	1/3	1/3
e–so	**y**	1/3	–	1/3
	z	1/3	1/3	–

directions are given in Table 12.3. The matrix elements averaged over all in-plane directions for TE-polarization are $3/2M_b^2$ ($1/2M_b^2$) for the electron to heavy (light) hole transition. For TM polarization the values are 0 and $2M_b^2$, respectively [1047]. The optical selection rules are shown in Fig. 12.29 (see Fig. 9.9 for bulk material). For propagation along the quantum-well plane, the ratio between the strength of the TE polarized e–hh and e–lh transitions is 3:1.

The confinement potential squeezes charge carriers bound to impurities closer to the ion. Therefore, the binding energy increases as shown in Fig. 12.30. This behavior can be modeled theoretically with good precision. It makes a difference whether the impurity is located at the center or the interface of the quantum well.

The confinement potential also squeezes electrons and holes in the exciton closer together and thus increases their Coulomb interaction. The binding energy of the quantum-well exciton is thus larger than in bulk material and depends on the well

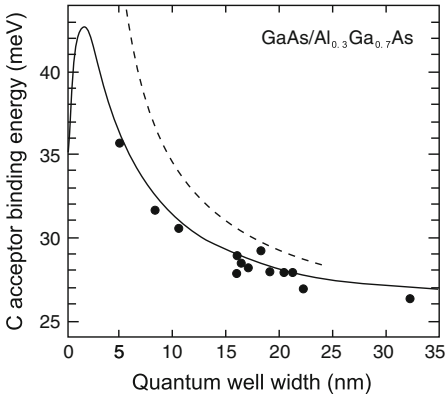

Fig. 12.30 Experimental values for the acceptor binding energy in $GaAs/Al_{0.3}Ga_{0.7}As$ quantum wells (*solid circles*) from [1048] as a function of well width. *Solid line* is theory (variational calculation) for the well-center acceptor including top four valence bands and finite barriers, *dashed line* is hydrogen-like model with infinite barrier height. Adapted from [1049]

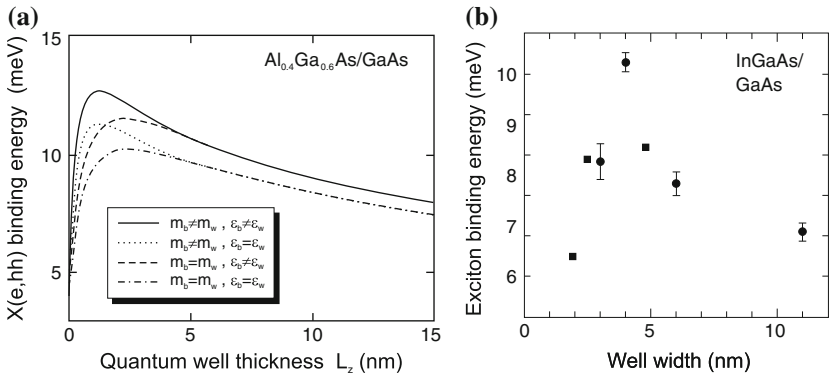

Fig. 12.31 (**a**) Theoretical (variational) calculation (*solid line*) of the heavy-hole exciton binding energy versus QW thickness in a $GaAs/Al_{0.4}Ga_{0.6}As$ quantum well (using also different approximations, *other lines*). Adapted from [1050]. (**b**) Experimental exciton binding energy in $In_xGa_{1-x}As/GaAs$ quantum wells of different thickness. *Circles*: data and error bars from [1051], x unspecified, *squares*: data from [1052], $x = 0.18$

width (Fig. 12.31). In the simple hydrogen-like model with infinite barriers the exciton binding energy is 4 times the bulk binding energy in the limit $L_z \to 0$. In a realistic calculation the effect of different dielectric constants in the well and barrier (image charge effect) need to be considered.

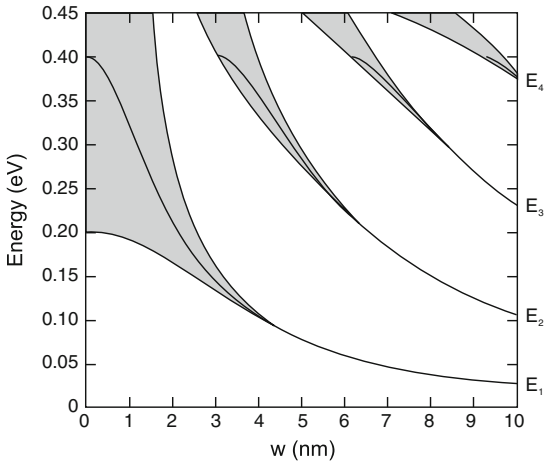

Fig. 12.32 Band structure of a superlattice with a potential depth of 0.4 eV and well and barrier width w ($L_{QW} = L_{barr}$). Adapted from [1053]

12.3.3 Superlattices

In a superlattice, the barrier thickness is so small that carriers can tunnel in neighboring wells or, in other terms, that there exists a significant wavefunction overlap between adjacent wells. This leads to a band structure (Fig. 12.32), similar to the Kronig–Penney model (Appendix F). For the superlattice the bands are called minibands, the gaps are called minigaps. The density of states does not make a step at the subband edge but follows an arccos function. The modification of the density of states, as seen in the absorption spectrum, are shown in Fig. 12.33 for 1, 2, 3 and 10 coupled wells.

12.3.4 Single Heterointerface Between Doped Materials

We consider a single heterointerface between n-doped materials. As an example we take n-AlGaAs/n-GaAs (Fig. 12.34). First, we consider the materials without contact, forming a type-I structure. In thermodynamic equilibrium the system must have a constant Fermi level. Thus, charge is transferred from the region close to the interface from AlGaAs to GaAs. This results in the formation of a triangular potential well in the GaAs close to the interface. A two-dimensional electron gas (2DEG) forms in this potential well (Fig. 12.35). The charge transfer in thermodynamic equilibrium adjusts the band bending and the charge density (quantized levels in the well) in such a way that they are self-consistent. The Poisson equation and the Schrödinger equation are simultaneously fulfilled. Numerically, both equations are iteratively solved and the solution is altered until it is self-consistent, i.e. it fulfills both equations.

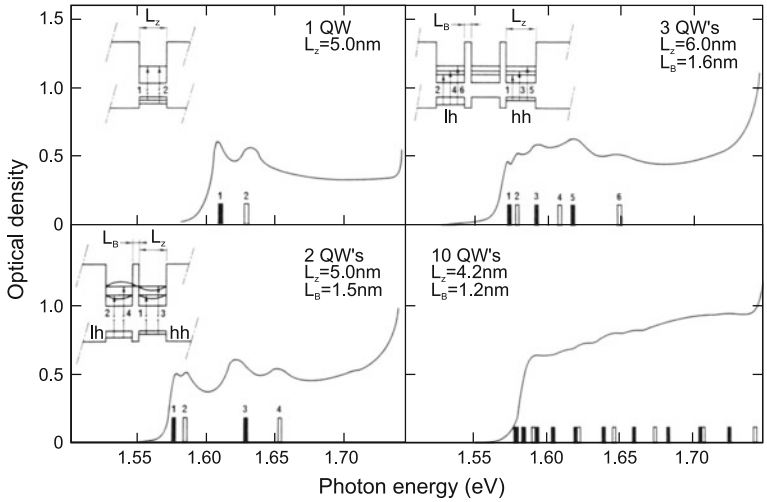

Fig. 12.33 Absorption spectra of a single, double, triple and ten coupled quantum wells. Theoretically predicted transitions with heavy (light) holes are labeled with *filled* (*empty*) *bars* at their respective transition energies. Adapted from [1054]

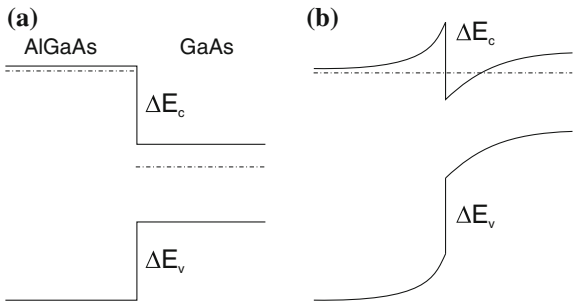

Fig. 12.34 Schematic formation of a triangular potential well in a n-AlGaAs/n-GaAs heterostructure, (**a**) before and (**b**) after equilibration of Fermi levels

If the region of the 2DEG is not doped, the electron gas exists without any dopant atoms and ionized impurity scattering no longer exists. This concept is called *modulation doping*. Mobilities up to 3.1×10^7 cm^2/Vs have been realized (Fig. 12.36). The theoretical limits of mobility in a 2DEG at modulation-doped AlGaAs/GaAs heterointerfaces are discussed in detail in [1056].

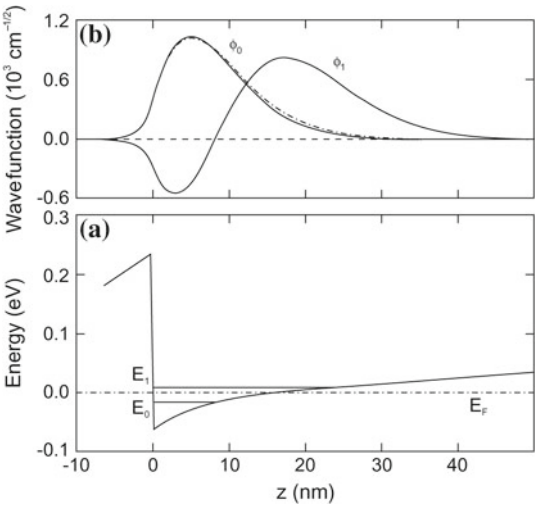

Fig. 12.35 (**a**) Conduction-band edge at a GaAs/$Al_{0.3}Ga_{0.7}As$ heterointerface ($T = 0$ K) with two confined states at E_0 and E_1 marked with *solid horizontal lines*. In the GaAs channel there are 5×10^{11} cm^{-2} electrons. The barrier height is 300 meV, $N_D^{GaAs} = 3 \times 10^{14}$ cm^{-3}. The position of the Fermi level E_F is at $E = 0$ and indicated with a *dash-dotted line*. (**b**) Envelope wavefunctions ϕ_0 and ϕ_1 of the two confined states, *dash-dotted line*: calculation without exchange and correlation for state at E_0. Adapted from [1055]

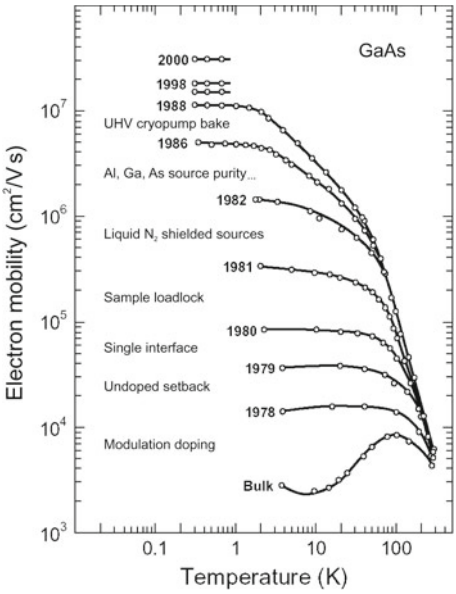

Fig. 12.36 Progress in the achievement of high electron mobility in GaAs, annotated with the technical innovation responsible for the improvement. Adapted from [1057]

12.4 Recombination in Quantum Wells

12.4.1 Thickness Dependence

The energy of exciton recombination in quantum wells is blue-shifted with respect to that in bulk material due to the quantum-confinement energies of electrons and holes (Fig. 12.37). The electron–hole recombination lineshape in quantum wells is given by the product of the joint density of states and the Boltzmann function (when Boltzmann statistics apply). The JDOS is given by a step function (Heavyside function $H(E)$).

$$I(E) \propto H(E - E_{11}) \exp\left(-\frac{E}{kT}\right), \tag{12.10}$$

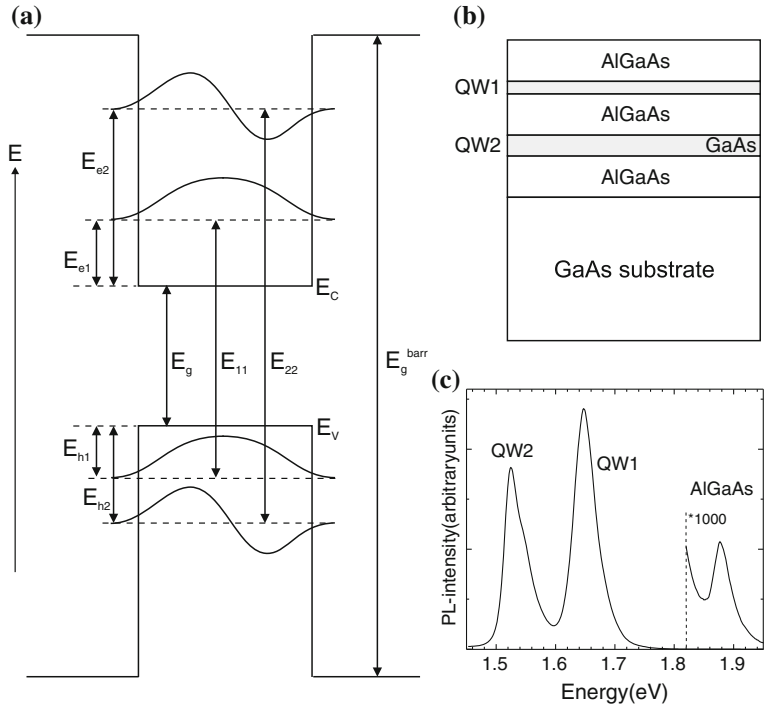

Fig. 12.37 (**a**) Schematic energy diagram of a quantum well with confined electron (e1, e2) and hole (h1, h2) states and recombination between them at energies E_{11} and E_{22}. (**b**) Schematic sample structure with two GaAs/$Al_xGa_{1-x}As$ quantum wells with thicknesses 3 and 6 nm. (**c**) Photoluminescence spectrum ($T = 300$ K) of the structure from part (**b**). A small amount of barrier luminescence appears at 1.88 eV, according to $x = 0.37$ (cf. Fig. 6.19c)

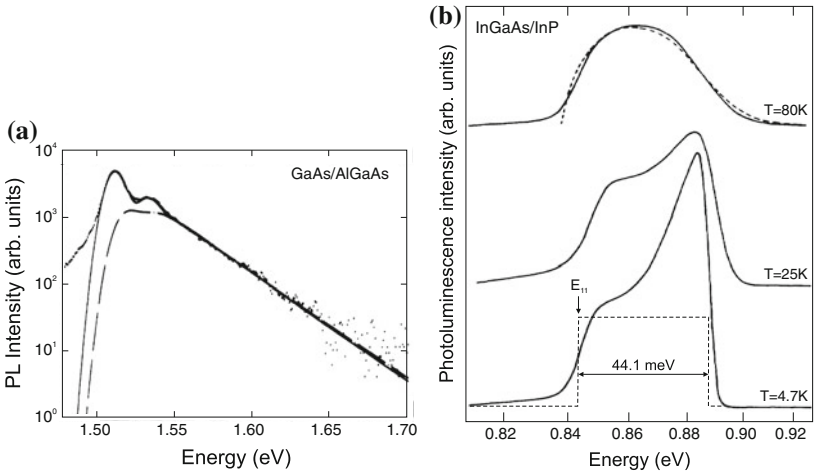

Fig. 12.38 (**a**) Reflectance spectra at various temperatures from a 17 nm thick GaAs/$Al_{0.3}Ga_{0.7}As$ quantum well. The *inset* shows the temperature dependence of the homogeneous linewidth. (**b**) LO phonon broadening parameter (FWHM) for various quantum well widths. Adapted from [1061]s

where $E_{11} = E_g + E_{e1} + E_{h1}$ represents the energy of the E1–H1 subband edge as shown in Fig. 12.37. An experimental spectrum (Fig. 12.39a) shows that excitonic effects influence the recombination lineshape in a GaAs quantum well even at room temperature [1058].

The recombination decay constant of excitons decreases with decreasing well width, partly due to the increase of exciton binding energy as discussed in [1059].

12.4.2 Broadening Effects

Many-Body Effects

At high carrier densities when the electron (quasi-) Fermi level is above the electron subband edge, the spectrum broadens and reflects the Fermi–Dirac distribution (Fig. 12.39b). At low temperatures a many-body effect, multiple electron–hole scattering with electrons at the Fermi edge, leads to an additional peak, termed *Fermi-edge singularity* that is discussed in [1060].

Homogeneous Broadening

The temperature dependence of the homogeneous broadening of quantum well luminescence has been investigated in [1061]. It follows the dependence of the broadening known from bulk material (Sect. 9.6.7) with similar values for the LO broadening parameter. In Fig. 12.38a the reflectance spectra for different temperatures of a 17 nm GaAs/$Al_{0.3}Ga_{0.7}As$ QW are shown. The optical phonon broadening parameter for various well widths is shown in Fig. 12.38b and coincides with the bulk value.

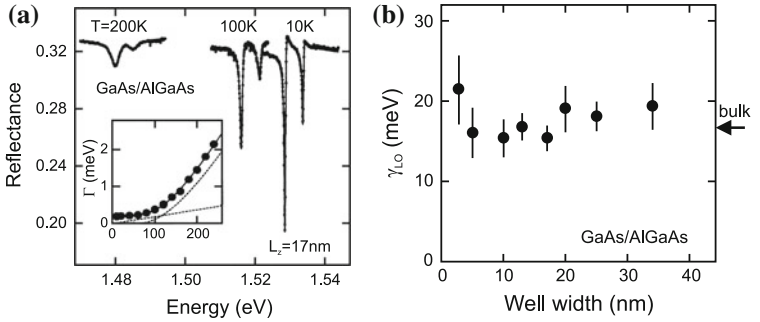

Fig. 12.39 (**a**) Photoluminescence spectrum of a 5-nm GaAs/AlGaAs quantum well at $T = 300\,\mathrm{K}$. The *solid* (*dashed*) line is fit with (without) excitonic effects. The two peaks are due to transitions involving heavy and light holes. Adapted from [1058]. (**b**) Photoluminescence spectra at three different temperatures as labeled of a 10-nm modulation-doped InGaAs/InP quantum well with an electron sheet density $n_s = 9.1 \times 10^{11}\,\mathrm{cm}^{-2}$. The electron quasi-Fermi level is $F_n - (E_C + E_{e1}) = 44.1\,\mathrm{meV}$ from the subband edge. The *dashed line* in the $T = 80\,\mathrm{K}$ spectrum is the lineshape from JDOS and a Fermi–Dirac distribution without enhancement at the Fermi edge. Adapted from [1060]

The homogeneous broadening leads to excitons with in-plane center-of-mass wave-vector $\mathbf{K} \neq 0$ being allowed to recombine radiatively. This leads to a linear increase of exciton lifetime as demonstrated for GaAs quantum wells up to 50 K in [1059]. In [1062] all exciton wave-vectors within the light cone are considered, explaining the linear increase of exciton lifetime in (non-polar) ZnO quantum wells up to room temperature.

Inhomogeneous Broadening

Inhomogeneous broadening affects the recombination lineshape. Since the interfaces of the QW are not ideally flat, the exciton averages over different quantum-well thicknesses within its volume. Also, e.g. for the GaAs/AlGaAs system, the wavefunction in the (binary) quantum well tunnels into the barrier, the amount depending on the QW width, and there 'sees' the alloy broadening (see Sect. 10.3.3). The problem of exciton dynamics in a potential with random fluctuations has been treated in detail [1063, 1064].

A simplified picture is as follows: At low temperatures the excitons populate preferentially the potential minima. A simple lineshape[5] of the QW absorption or joint density of states is given by a step function (cf. Table 9.2) at the QW band edge E_0. The inhomogeneous broadening has a Gaussian probability distribution $p(\delta E) \propto \exp[-(\delta E)^2/2\sigma^2)]$ with δE being the deviation from the QW band edge $\delta E = E - E_0$. The resulting lineshape is given by the convolution of the Gaussian

[5] neglecting excitonic enhancement.

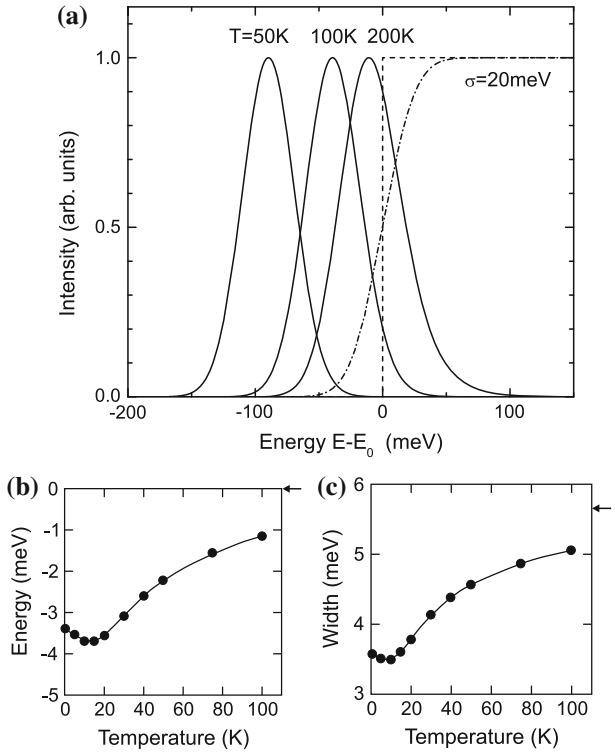

Fig. 12.40 (**a**) Recombination spectra (*solid lines*, scaled to same height) of a model quantum well for different temperatures as labeled and complete thermalization, *dashed* (*dash-dotted*) *line* is unperturbed (inhomogeneously broadened by $\sigma = 20\,\text{meV}$) shape of the QW absorption edge. The energy scale is relative to the energy position of the unperturbed QW absorption edge at E_0. (**b**) Theoretical energy position and (**c**) linewidth of exciton recombination from a model disordered quantum well. The high-temperature limits are marked by *arrows*. Parts (**b**, **c**) adapted from [1063]

with the unperturbed absorption spectrum yielding an error-function-like spectrum[6] as shown in Fig. 12.40a.

For complete thermalization the level population is given by the Boltzmann function. The recombination spectrum is given by the product of the absorption spectrum (or JDOS) and the Boltzmann function. It is (red-) shifted with respect to E_0 by about[7]

$$\Delta E(T) = -\frac{\sigma^2}{kT} = \gamma(T)\, kT. \tag{12.11}$$

This shift between emission and absorption is also called the Stokes shift.

[6]The error function is defined as $\text{erf}(x) = (2/\sqrt{\pi}) \int_0^z \exp -t^2 \, \text{d}t$.

[7]Formula (12.11) is exact for the product of a Gaussian and the Boltzmann function.

Within their lifetime, limited at least by radiative recombination, the excitons are typically unable to reach the energy position required by the Boltzmann function, but only a local minimum. Thus, their thermalization may be incomplete due to insufficient lateral diffusion. This effect is particularly important at low temperatures when thermal emission into adjacent deeper potential minima is suppressed. In this case, the red-shift is smaller than expected from (12.11). A numerical simulation [1063] yields such behavior of the energy position of the recombination line as shown in Fig. 12.40b. Simultaneously, the width of the recombination spectrum also exhibits a minimum (Fig. 12.40c). These findings are in agreement with experiments [1065, 1066]. An analytical model for temperature dependent exciton localization in the presence of disorder has been given in [1067], yielding a value $0 \leq \gamma \leq \gamma_0 = (\sigma/kT)^2$ in (12.11).

A potential fluctuation can localize an exciton laterally at low temperatures [1058] and behave like a quantum dot (cf. Sect. 14.3). Localized and delocalized excitons are separated by a boundary called the mobility edge [1068]. The transition between the two regimes is a Mott transition [1069].

Monolayer Growth Islands

Under certain growth conditions, quantum wells with piecewise very flat interfaces can be fabricated. The thickness difference between such regions (with lateral extension in the μm range) is an integer monolayer. Accordingly, the recombination spectrum yields several, typically two or three, discrete lines (Fig. 12.41).

12.4.3 Quantum Confined Stark Effect

The quantum confined Stark effect (QCSE, Sect. 13.1.2) in quantum wells shifts energy levels when electric fields are present along the width of the quantum well. A strong effect exists for pyro- and piezoelectric material combinations such as *c*-axis oriented (In,Ga)N/(Al,Ga)N [1070, 1071] or (Cd,Zn)O/(Mg,Zn)O [1072, 1073] quantum wells due to the built-in electric field (cf. Sect. 15.2). The QCSE induced red-shift is larger in thicker quantum wells and goes beyond the bulk band gap of the quantum well material (Fig. 12.42b). Also the wavefunction overlap is reduced with increasing well width, leading to an increase of the radiative recombination lifetime as shown in Fig. 12.42. The pyroelectric field and the related modification of lifetime are absent in quantum wells grown on non-polar directions such as [11.0] (Fig. 12.42a).

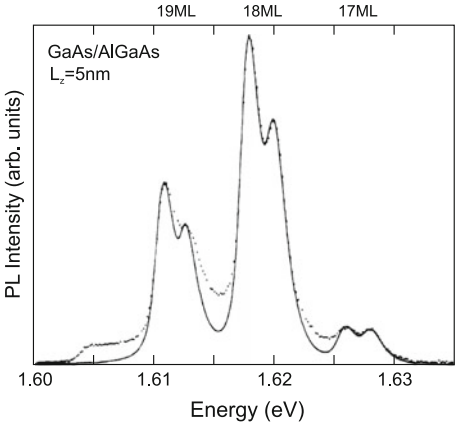

Fig. 12.41 Photoluminescence spectrum ($T = 2\,\mathrm{K}$) (*dots*) of GaAs/AlGaAs quantum well grown by MBE with 120 s growth interruptions. Recombination is due to excitons in islands of 19, 18, and 17 monolayers ($a_0/2$) height. The *solid line* is a lineshape fit including lifetime broadening ($\Gamma = 1.34\,\mathrm{meV}$) and residual inhomogeneous broadening ($\sigma = 0.04\,\mathrm{meV}$) due to AlGaAs barrier alloy fluctuations. Note that the energy separation of the peaks is much larger than kT. The peak doublet structure is discussed in [1058]. Adapted from [1058]

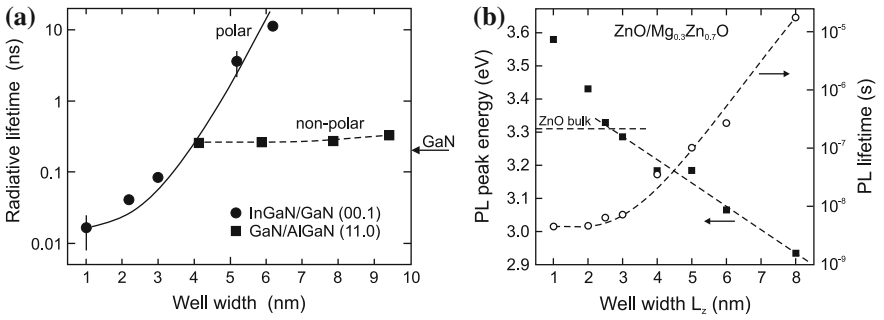

Fig. 12.42 (**a**) Radiative lifetime of electron-hole pairs in polar [00.1]-oriented $In_{0.2}Ga_{0.8}N$/GaN (*circles*) and non-polar [11.0]-oriented GaN/$Al_{0.2}Ga_{0.8}N$ (*squares*) quantum wells of varying thickness. Experimental data are shown in *symbols*. The *solid line* is the (scaled) theoretical dependence of the electron-hole overlap for (In,Ga)N/GaN QWs. The *dashed line* is guide to the eyes. The *arrow* denotes the recombination time constant in bulk GaN. Adapted from [1074, 1075]. (**b**) Low temperature PL peak recombination energy (*solid squares*) for ZnO/$Mg_{0.3}Zn_{0.7}O$ quantum wells for various well widths L_z (barrier width $L_B = 5\,\mathrm{nm}$). *Dashed line* indicates dependence for internal field of 0.9 MV/cm, *horizontal dashed line* indicates recombination energy in ZnO bulk. Carrier lifetime determined from PL (*circles*), *dashed line* is guide to the eyes. Adapted from [1073]

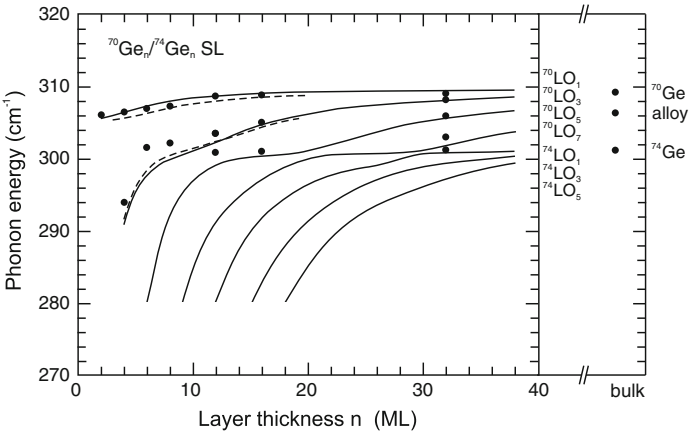

Fig. 12.43 Measured (*full circles*) and theoretical (*solid lines*) confined LO phonon energies in $^{70}Ge_n/^{74}Ge_n$ superlattices versus the layer thickness (number of monolayers) n. The *dashed lines* represent a calculation that considers intermixing at the interfaces. On the right, the energies of bulk modes for isotopically pure ^{70}Ge and ^{74}Ge are shown together with that of an $^{70}Ge_{0.5}{}^{70}Ge_{0.5}$ alloy. Adapted from [1076]

12.5 Isotope Superlattices

A special type of heterostructure is the modulation of the isotope content. The first kind of heterostructures made like this were $^{70}Ge_n/^{74}Ge_n$ symmetric superlattices [1076]. Figure 12.43 shows phonon energies determined from Raman spectroscopy for various layer numbers n. The modes are classified by $^{70}LO_m$ and $^{74}LO_m$ denoting the material in which the amplitude is maximal and m being the number of maxima in that medium.[8] Such modes are visualized in Fig. 12.44a for a $^{69}GaP_{16}/^{71}GaP_{16}$ superlattice. Theoretical mode energies as a function of the superlattice period are shown in Fig. 12.44b.

12.6 Wafer Bonding

Wafer bonding is a fairly recently developed method to join different and dissimilar materials. Two wafers of the respective materials are put together face to face and are adequately fused. The idea is to not only 'glue' the wafers together with a sticky (and compliant) organic material, but to form strong atomic bonds between the two materials with possibly a perfect interface. In some cases, the interface needs to allow charge-carrier transport through it. Less stringent conditions need to be met for photon transport.

[8] Only modes with odd m are Raman-active.

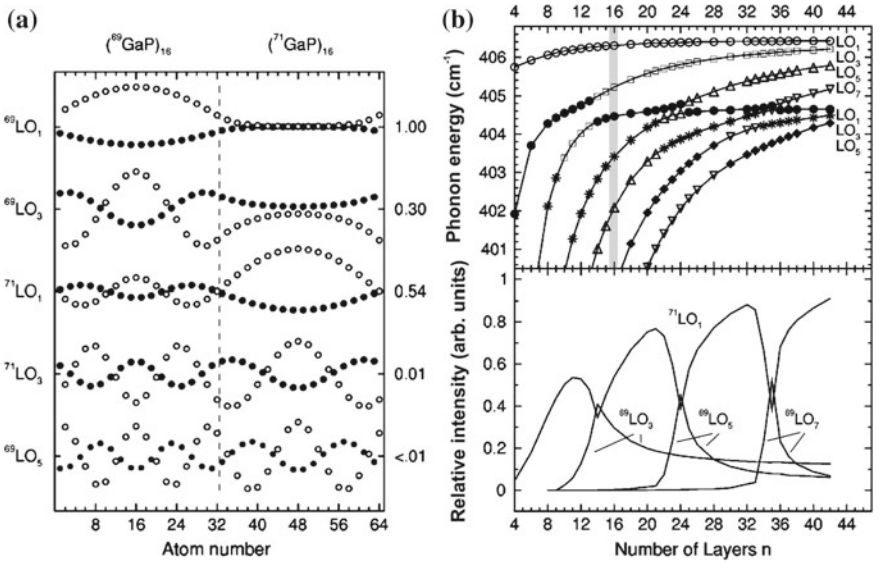

Fig. 12.44 (**a**) Atomic displacements [Ga (*filled dots*) and P (*open circles*)] of odd-index LO modes in a $^{69}Ga_{16}P/^{71}Ga_{16}P$ superlattice unit cell. These modes have even parity with respect to midlayer planes, which are at atom numbers 16 and 48 in this example. The labels on the *left* identify the predominant character of the mode, those on the *right* give the relative Raman intensities with respect to that of the $^{69}LO_1$ mode. The tick marks on the vertical axis indicate zero displacement of the respective mode. (**b**) *Upper panel*: Energies and characters of odd-index LO phonon modes in GaP isotope SLs as calculated within the planar bond charge model for the case of ideal interfaces. $^{69}LO_m$ modes are shown as *open symbols*; $^{71}LO_m$ modes as *full symbols*. The *shaded area* marks $n = 16$ for which the atomic displacements of the modes are shown in part (**a**). *Lower panel*: Calculated intensities of the modes relative to that of the $^{69}LO_1$ phonon mode. Adapted from [335], reprinted with permission, © 1999 APS

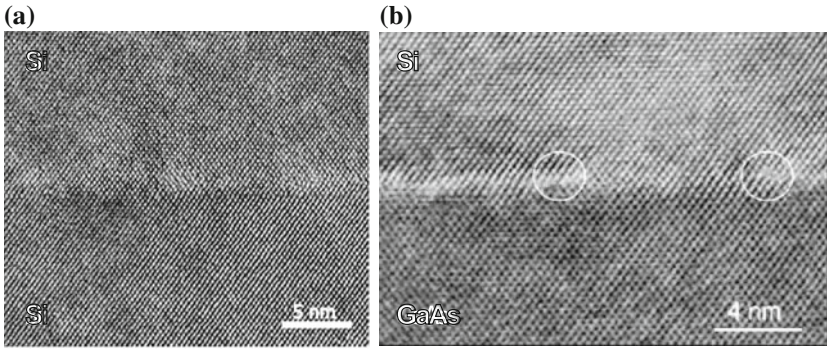

Fig. 12.45 High-resolution TEM images of wafer-bonded (**a**) Si-Si and (**b**) GaAs-Si interfaces. *White circles* indicate the position of misfit dislocations. Part (**a**) reprinted from [1077], © 2003, with permission from Elsevier. Part (**b**) reprinted with permission from [1078], © 1998 AIP

Mechanical deficiencies such as surface roughness, dust particles and the like must be avoided in the wafer-bonding process since they result in voids. Several methods have been developed for bonding various materials [1079, 1080]. Such processes are successful for large substrate sizes. With proper processing, ideal interfaces can be created, as shown in Fig. 12.45. Such structures, if made between a p-doped and a n-doped semiconductor, show diode characteristics.